Molecular Therapy
Nucleic Acids
Original Article

Efficacy and safety of a SOD1-targeting artificial miRNA delivered by AAV9 in mice are impacted by miRNA scaffold selection

Shukkwan K. Chen,[1,3] Zachary C.E. Hawley,[1,3] Maria I. Zavodszky,[1] Sam Hana,[1] Daniel Ferretti,[1] Branka Grubor,[1] Michael Hawes,[2] Shanqin Xu,[1] Stefan Hamann,[1] Galina Marsh,[1] Patrick Cullen,[1] Ravi Challa,[1] Thomas M. Carlile,[1] Hang Zhang,[1] Wan-Hung Lee,[1] Andrea Peralta,[1] Pete Clarner,[1] Cong Wei,[1] Kathryn Koszka,[1] Feng Gao,[1] and Shih-Ching Lo[1]

[1]Biogen, Cambridge, MA, USA; [2]Charter Preclinical Services, Hudson, MA, USA

Toxic gain-of-function mutations in superoxide dismutase 1 (SOD1) contribute to approximately 2%–3% of all amyotrophic lateral sclerosis (ALS) cases. Artificial microRNAs (amiRs) delivered by adeno-associated virus (AAV) have been proposed as a potential treatment option to silence SOD1 expression and mitigate disease progression. Primary microRNA (pri-miRNA) scaffolds are used in amiRs to shuttle a hairpin RNA into the endogenous miRNA pathway, but it is unclear whether different primary miRNA (pri-miRNA) scaffolds impact the potency and safety profile of the expressed amiR *in vivo*. In our process to develop an AAV amiR targeting SOD1, we performed a preclinical characterization of two pri-miRNA scaffolds, miR155 and miR30a, sharing the same guide strand sequence. We report that, while the miR155-based vector, compared with the miR30a-based vector, leads to a higher level of the amiR and more robust suppression of SOD1 *in vitro* and *in vivo*, it also presents significantly greater risks for CNS-related toxicities *in vivo*. Despite miR30a-based vector showing relatively lower potency, it can significantly delay the development of ALS-like phenotypes in SOD1-G93A mice and increase survival in a dose-dependent manner. These data highlight the importance of scaffold selection in the pursuit of highly efficacious and safe amiRs for RNA interference gene therapy.

INTRODUCTION

Amyotrophic lateral sclerosis (ALS), also known as Lou Gehrig's disease, is a chronic and progressive disease leading to deterioration of the upper and lower motor neurons in the brain and spinal cord, respectively.[1] Approximately 18.9% of familial ALS and 1.2% of sporadic ALS cases contain mutations resulting in a toxic gain-of-function of superoxide dismutase 1 (SOD1).[2,3] Several animal models with SOD1 gain-of-function mutations result in ALS-like phenotypes, including mitochondrial dysfunction, SOD1 protein aggregation, motor neuron death, and reduced motor function, and thereby provide a causal link between mutant SOD1 and ALS.[4–7] It has been shown that suppressing *SOD1* gene expression through RNA interference (RNAi) can alleviate ALS-like pathology and improve survival in SOD1-ALS preclinical models.[8–10] Thus, reducing levels of SOD1 is predicted to be therapeutic and is being investigated in the clinic.[11,12]

Recombinant adeno-associated virus (AAV)-mediated delivery of RNAi agents, including artificial microRNAs (amiRs), in the CNS to achieve long-term SOD1 suppression and preservation of neuronal function is an alluring clinical approach.[12] Artificial miRNAs consist of a short interfering RNA inserted into a primary miRNA (pri-miRNA) scaffold, allowing it to utilize the endogenous miRNA system (reviewed in Kotowska-Zimmer et al., 2021).[13] Similar to endogenous miRNAs, once expressed, amiRs are first processed by Drosha ribonuclease III (DROSHA) in the nucleus and subsequently by Dicer ribonuclease III (DICER) in the cytoplasm, creating a miRNA duplex that contains a guide and passenger strand. The guide strand is loaded into argonaute 2, activating the RNA-induced silencing complex, leading to gene silencing, while the passenger strand usually gets degraded.[14] When stably expressed from a viral vector, amiRs are continuously processed by the endogenous miRNA pathway and provide long-lasting silencing of toxic genes, making it an attractive therapeutic approach for patients with SOD1-ALS.[12]

However, there are growing reports of RNAi-associated toxicity *in vivo* when delivered from AAV vectors as an intended gene therapy. This toxicity could be due to processing competition between amiRs and the endogenous miRNAs, resulting in oversaturation of the endogenous miRNA biogenesis pathway.[15–17] To achieve optimal expression of an amiR while avoiding potential toxicities, multiple components of the AAV construct, including scaffolds, serotypes, promoters, cis-regulatory elements, and dosage, can be fine tuned.[17] For example, when an amiR targeting the human *HTT* gene, encoding huntingtin, was expressed with a polymerase III (Pol III) promoter

Received 27 September 2022; accepted 12 October 2023;
https://doi.org/10.1016/j.omtn.2023.102057.

[3]These authors contributed equally

Correspondence: Shih-Ching Lo, Biogen, 225 Binney Street, Cambridge, MA, USA.
E-mail: joyce.lo@biogen.com

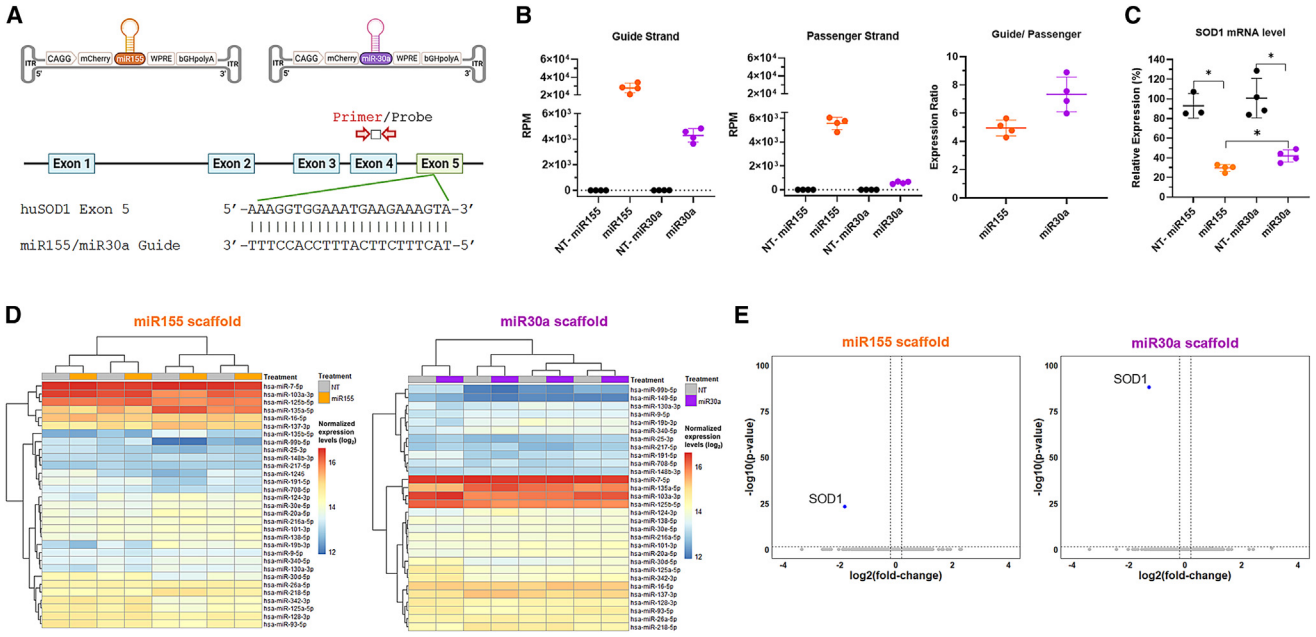

Figure 1. AAV9-miR155-SOD1 shows greater artificial miRNA expression than AAV9-miR30a-SOD1 *in vitro*

(A–E) NGN2 neurons were transduced with an artificial miRNA targeting SOD1 that was inserted into either a miR155 or miR30a scaffold, and a non-targeting (NT) control into the same scaffolds. Samples were analyzed 14 days post-transduction. (A) Illustration of artificial miRNA vectors and the complementary guide strand sequence targeting SOD1 (exon 5) and PCR amplicon targeting SOD1 (exon 4). (B) Reads per million (RPM) of artificial miRNA guide and passenger strands when expressed in either a miR155 scaffold or a miR30a scaffold as calculated by small RNA-seq. Data presented as mean ± SD (n = 4). (C) Real-time PCR shows percent SOD1 expression compared with NT control after artificial miRNA treatment. Expression levels were normalized to GAPDH prior to comparison. Data presented as mean ± SD (n = 4). Welch's one-way ANOVA followed by Holm-Sidak's multiple comparison post hoc (*$p < 0.05$). (D) Heatmap of the top 30 expressing endogenous miRNAs in NGN2 neurons. Values in the heatmap represent log2 (RPM) (n = 4). (E) Differential mRNA expression in NGN2 neurons after artificial miRNA treatment based on RNA-seq analysis (n = 4). Two-tailed Wald test and p values were adjusted for multiple comparisons by implementing Benjamini-Hochberg false discovery rate. Blue dots indicate significant changes and gray dots highlight non-significant changes in transcript expression compared with control.

and delivered to the mouse striatum, it resulted in microglial activation, striatal damage, and behavioral abnormalities. These adverse events were avoided when the same amiR was expressed from a weaker polymerase II (Pol II) promoter.[18] Therefore, a thorough understanding of the amiR safety profile is imperative to further RNAi constructs.

In part of our development to design an AAV amiR-targeting SOD1, we examined how two pri-miRNA scaffolds (miR30a and miR155) differed in the processing and production of an amiR that contained the same SOD1-targeting sequence. The miR155-based vector achieved higher guide strand production and SOD1 suppression in human iPSC-derived NGN2 neurons, mouse brain, and mouse spinal cord compared with the miR30a-based vector. However, the miR155 scaffold led to a notable increase in neurodegeneration events in multiple CNS regions in the wild-type mice. In contrast, the miR30a scaffold resulted in only minimal to mild changes in the peripheral nerves *in vivo*. Despite lower production of amiR from the miR30a scaffold, we demonstrated that the miR30a-based vector can still effectively delay the development of ALS-like phenotypes and prolong survival in SOD1-G93A mice in a dose-dependent manner. These findings address the potential toxic characteristics of specific pri-miRNA scaffolds and contribute to the knowledge of vector design and safety profiling in using amiRs as an effective RNAi shuttle.

RESULTS

Effects of different pri-miRNA scaffold-based vectors on amiR expression and function *in vitro*

First, we wanted to determine the impact of two pri-miRNA scaffolds (miR155 and miR30a) on amiR expression and whether these differences impact the potency of SOD1 suppression. AAV9 vectors contained the same SOD1-targeting amiR inserted into either a miR155 (AAV9-miR155-SOD1) or miR30a (AAV9-miR30a-SOD1) pri-miRNA scaffold expressed through a Pol II CAGG promoter (Figure 1A). Both vectors showed comparable transduction efficiency and viral load within human iPSC-derived NGN2 neurons (Figures S1 and S2). At 14 days post-transduction, AAV9-miR155-SOD1 resulted in a 6-fold increase in guide strand production compared with AAV9-miR30a-SOD1 as quantified by small RNA sequencing (RNA-seq). Both vectors showed guide-to-passenger strand ratios of approximately 5 and approximately 7 for AAV9-miR155-SOD1 and AAV9-miR30a-SOD1, respectively (Figure 1B). Since miRNAs can produce alternative isoforms (isomiRs) due to shifts in DROSHA and DICER cleavage or nucleotide additions at the 3′ end,[19] we

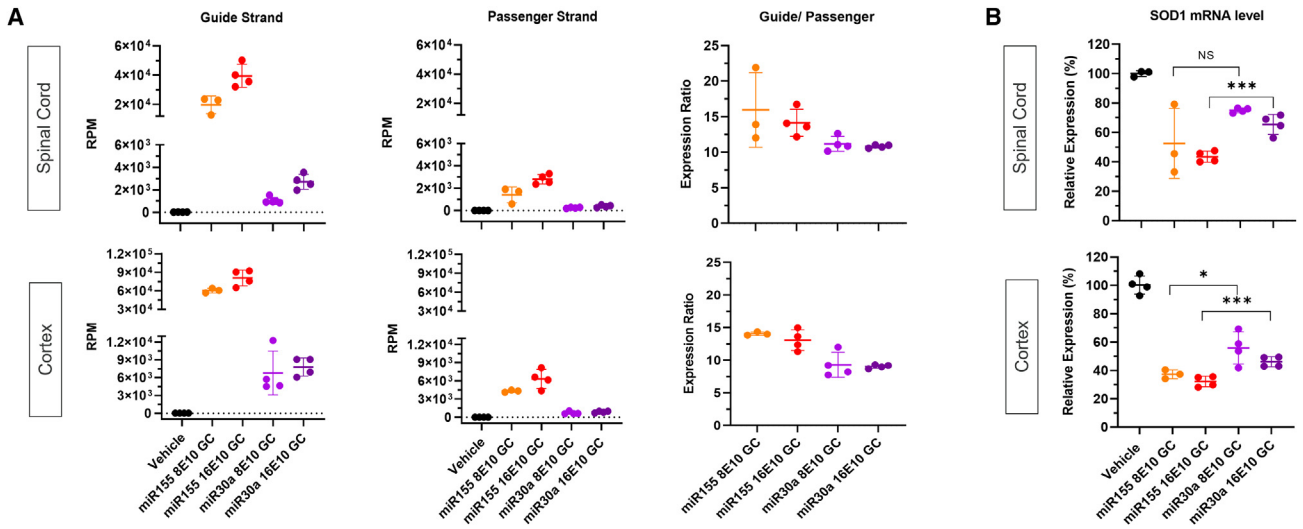

Figure 2. AAV9-miR155-SOD1 shows greater artificial miRNA expression than AAV9-miR30a-SOD1 *in vivo*

(A and B) Mice were given a P0 ICV injection of either AAV9-miR155-SOD1, AAV9-miR30a-SOD1, or a vehicle control. Each amiR was given at two different dose levels, 8E+10GC or 16E+10GC. Expression levels of the artificial miRNA were measured 10 weeks post-injection. (A) RPM of artificial miRNA guide and passenger strands when expressed in either the miR155 or miR30a scaffold in the spinal cord and cortex using small RNA-seq. (B) qPCR shows percent SOD1 expression compared with control in the spinal cord or cortex after artificial miRNA treatment. SOD1 levels were normalized to GAPDH levels prior to comparison. Data presented as mean ± SD (n = 3–4). Generalized least squares test followed by a Tukey's post hoc to adjust for multiple comparisons ($^{NS}p > 0.05$, $^{*}p < 0.05$, $^{***}p < 0.001$).

examined whether the two different scaffolds impacted isomiRs for the amiR. The predicted isoform of the guide strand is 21 nucleotides in length, but 3′ end extensions resulted in predominately 22 and 24 nucleotide isomiRs from the miR30a-based and miR155-based vector, respectively (Figure S3). IsomiRs with mismatch sequences in the canonical region were infrequently observed for either vector (Figure S4). These data indicate that pri-miRNA scaffolds can impact isomiR formation, particularly with 3′ extensions.

qPCR determined that AAV9-miR30a-SOD1 reduced SOD1 levels by 58.9% as compared with the non-targeting control, but AAV9-miR155-SOD1 had a slight yet significantly greater suppressive effect, reducing SOD1 levels by 63.3% (Figure 1C). Further, transduction of AAV9-miR30a-SOD1 or AAV9-miR155-SOD1 into primary cortical neurons results in 70%–75% reduction of SOD1 protein in miR30a- and miR155-scaffold, respectively (Figure S5). Expression of these amiR vectors showed no evidence of saturation in endogenous miRNA pathway as small RNA-seq showed no significant changes in endogenous miRNA expression (data not shown). Also, heatmaps highlighting the top 30 most abundant endogenous miRNAs revealed limited and insignificant variations across treatment groups (Figure 1D). Last, it is important to note that amiR-mediated gene silencing is highly specific to human SOD1 in iPSC-derived NGN2 cells, regardless of the pri-miRNA scaffold used. The mRNA-seq analysis revealed no statistically significant transcriptomic changes other than a robust knockdown of SOD1 (Figure 1E). These data suggest both miRNA-based vectors are highly specific in silencing SOD1 expression and have no impact on endogenous miRNA production.

Effects of different pri-miRNA scaffold-based vectors on amiR expression and function *in vivo*

After determining the differences between the miR155 and miR30a scaffolds in amiR expression and potency *in vitro*, we wanted to evaluate how these differences translated into an *in vivo* setting. Postnatal day 0 (P0) ICV injections into mice were performed by administering either vehicle control, AAV9-miR155-SOD1, or AAV9-miR30a-SOD1 at two dose levels: 8E+10GC and 16E+10GC. At 10 weeks of age, vectors showed comparable viral loads in the cortex and spinal cord (Figure S6), and amiR expression correlated with viral load (Figure S7). The most abundant isomiR observed from each vector in mouse CNS tissue is similar to that observed *in vitro* (Figures S3 and S4). Guide-to-passenger strand ratios were more than 10, independent of the dose levels used. Strikingly, at both dose levels, AAV9-miR155-SOD1 resulted in approximately 10-fold higher guide strand production than the AAV9-miR30a-SOD1 in both the spinal cord and cortex (Figure 2A). Examination of the different vector components (mCherry and WPRE) revealed slightly higher expression of these two components by approximately 2-fold in mice treated with the miR30a-based vector compared with the miR155-based vector in both cortex and spinal cord (Figure S8), suggesting the approximately 10-fold higher guide strand production seen with the miR155 scaffold is unlikely caused by variation in overall cargo expression or ICV injection.

In turn, AAV9-miR155-SOD1 resulted in a significantly greater knockdown of SOD1 expression in CNS tissue than AAV9-miR30a-SOD1. However, this difference in suppression was not 10-fold as expected, based on differences in guide strand production

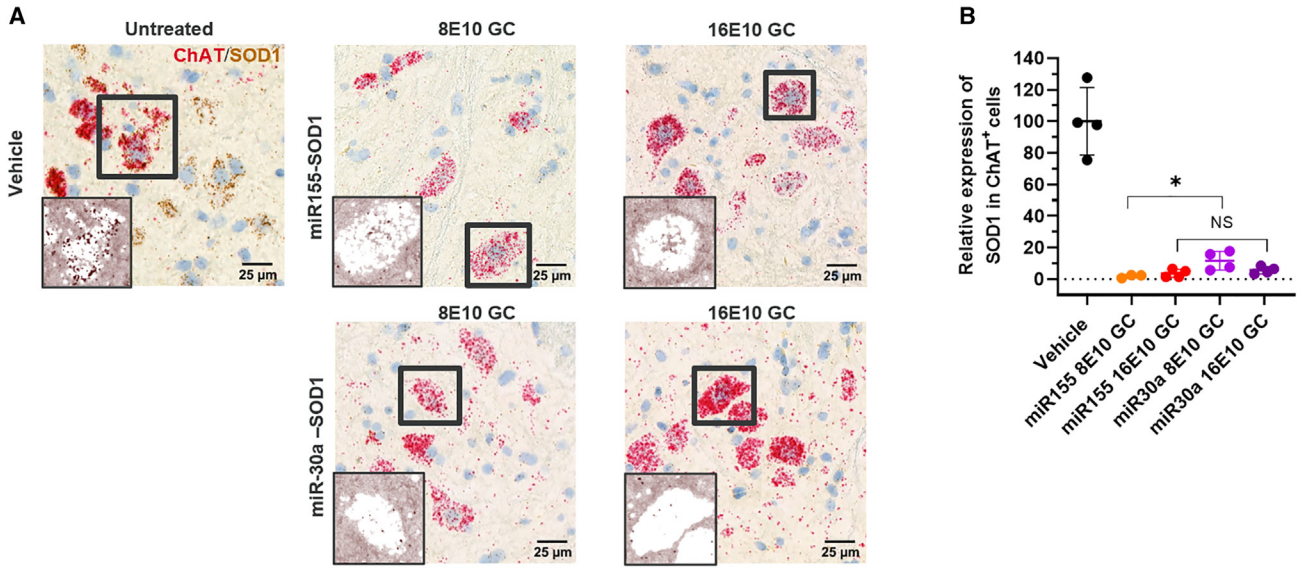

Figure 3. Suppression of SOD1 in spinal motor neurons after AAV9-amiR-SOD1 treatment

(A and B) Mice were given a P0 ICV injection of either AAV9-miR155-SOD1, AAV9-miR30a-SOD1, or vehicle control. Each amiR was given at two different dose levels, 8E+10GC or 16E+10GC. Expression of SOD1 was measured in motor neurons 10 weeks post-injection. (A) RNA scope showing ChAT+ (red) and SOD1+ (brown) cells. Black boxes indicate regions shown at 40x optical magnification illustrating SOD1+ (brown) chromogen. (B) Percent SOD1 in ChAT+ cells after treatment. Percentage SOD1 in ChAT+ cells was normalized to the vehicle prior to comparison. Data presented as mean ± SD (n = 3–4). Generalized least squares test followed by a Tukey's post hoc test to adjust for multiple comparisons ($^{NS}p > 0.05$, $^{*}p < 0.05$).

between the two vectors. Instead, AAV9-miR155-SOD1 showed a approximately 47% and approximately 56% reductions of SOD1 in the spinal cord and approximately 62% and approximately 68% reductions of SOD1 in the cortex at a low (8E+10GC) and high (16E+10GC) dose, respectively, whereas AAV9-miR30a-SOD1 showed approximately 25% and approximately 34% reductions of SOD1 in the spinal cord and approximately 44% and approximately 54% reductions of SOD1 in the cortex at a low (8E+10GC) and high (16E+10GC) dose, respectively (Figure 2B). RNA-seq confirmed similar reductions of SOD1 within these bulk CNS tissue samples (data not shown). Therefore, we observe modest yet significant improvements in SOD1 suppression in the CNS tissue of mice when the amiR is inserted into a miR155 scaffold rather than a miR30a scaffold.

Since motor neurons are primarily impacted within SOD1-ALS and AAV9 has been shown to efficiently target motor neurons within the CNS,[20] we next investigated SOD1 suppression in mouse spinal motor neurons using *in situ* hybridization techniques. There was almost a complete knockdown of SOD1 mRNA (>98%) in spinal motor neurons after AAV9-miR155-SOD1 treatment, even at a low dose (8E+10GC), while AAV9-miR30a-SOD1 achieved approximately 88% knockdown at the same dose. However, both vectors resulted in a 94%–96% knockdown at a high dose (16+E10GC), showing no significant difference in potency (Figure 3). These data indicate that, despite yielding a 10-fold higher expression level of the guide strand, the miR155-based vector only showed modest improvement in potency when compared with the miR30a-based vector *in vivo*.

Effects of different pri-miRNA scaffolds on vector safety profile *in vivo*

Next, we wanted to determine whether treatment with these vectors resulted in adverse events. Histopathology revealed minimal to moderate axonal degeneration within the dorsal funiculus of the spinal cord and sciatic nerve when mice were treated with AAV9-miR155-SOD1. However, animals treated with AAV9-miR30a-SOD1 showed none to mild axonopathy. Most strikingly, high dose (16E+10GC) levels of AAV9-miR155-SOD1 resulted in Purkinje neuron loss in the cerebellar folia. This was not observed in mice treated with AAV9-miR30a-SOD1 at the same dose level (Figures 4A and 4B).

Measuring of serum neurofilament is an effective strategy to assess potential neurotoxic events in rodents, as there is a direct correlation between serum neurofilament levels and axonal injury.[21] Therefore, we decided to assess whether the more severe pathology observed in AAV9-miR155-SOD1 treated animals corresponded with greater increases in serum phosphorylated neurofilament heavy subunit (pNF-H). In comparison with vehicle control-treated mice, serum pNF-H concentrations were significantly elevated at 5 and 9 weeks after injection with AAV9-miR155-SOD1 treatment at either dose, but not when mice were treated with AAV9-miR30a-SOD1 at the same dose levels. This indicates that the miR155-based vector induced more severe neurotoxic events, consistent with histopathology (Figure 4C). Furthermore, approximately 40%–50% of AAV9-miR155-SOD1 treated mice showed a decreased life span before reaching 150 days of age. In contrast, similar to C57BL/6J mice reported in

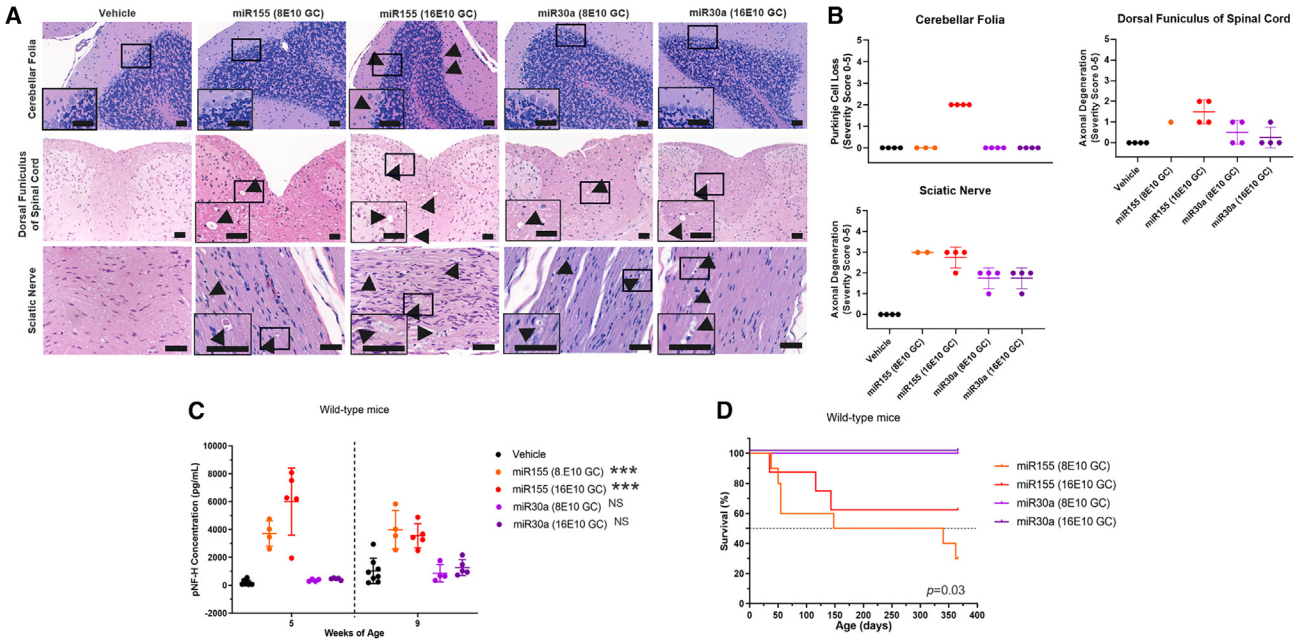

Figure 4. A greater number of adverse events are associated with the miR155 scaffold than with the miR30a scaffold

(A–D) Mice were given a P0 ICV injection of either AAV9-miR155-SOD1, AAV9-miR30a-SOD1, or vehicle control. Each amiR was given at two different dose levels, 8E+10GC or 16E+10GC. (A) H&E staining highlighting various pathologies associated with either AAV9-miR30a-SOD1 or AAV9-miR155-SOD1 treatment within the sciatic nerve, spinal cord, or cerebellum. Scale bars represent 50 μm. (B) Scatterplot representing pathological severity related to AAV9-amiR-SOD1 treatment. (C) A longitudinal measure of serum pNF-H levels in mice. Data presented as mean ± SD (n = 4–8). Significance versus vehicle was determined using a generalized estimating equation (***p < 0.001). (D) Survival of mice after AAV-amiR treatment (n = 4–10). Log rank test was used to determine if there was evidence in favor of a different survival between groups (p = 0.03).

the literature,[22] AAV9-miR30a-SOD1-treated mice displayed a normal life span before the study was terminated at the 1-year mark (Figure 4D). Therefore, by changing the pri-miRNA scaffold from miR155 to miR30a without altering the guide strand sequence, we were able to mitigate neurotoxicity and improve the safety profile of the vector in mice.

AAV9-miR30a-SOD1 reduces ALS-like phenotypes in SOD1-G93A mice

Since AAV9-miR30a-SOD1 exhibited a more favorable safety profile, we sought to evaluate whether the treatment of AAV9-miR30a-SOD1 could alleviate disease progression in SOD1-G93A mice. AAV9-miR30a-SOD1 was administered to SOD1-G93A mice through a P0 ICV injection at five different doses (0.5E+10GC, 1.5E+10GC, 4E+10GC, 8E+10GC, and 16E+10GC). Elevated serum neurofilament, including pNF-H, is a known by-product of axonal damage. It has been shown to be an effective serum and cerebrospinal fluid biomarker for neurodegenerative diseases, including ALS.[23,24] Additionally, preclinical models of ALS, such as SOD1-G93A mice, also contain elevated serum neurofilament; thus, this biomarker can be used as one measurement to assess the efficacy of a drug in preventing neurodegeneration in a preclinical setting.[25] In our study, SOD1-G93A mice treated with AAV9-miR30a non-targeting control showed mean serum pNF-H levels of 11169.86 pg/mL, which was approximately 10-fold greater than the average pNF-H levels observed in wild-type mice (1,032.49 pg/mL) (Figure 4C). We quantified serum pNF-H in our treated animals and observed a dose-dependent decrease in serum pNF-H levels in SOD1-G93A mice treated with AAV9-miR30a-SOD1 compared with mice treated with AAV9-miR30a non-targeting control at 21 week post-injection. Furthermore, mice in the two highest dose groups (8E+10GC and 16E+10GC) who survived up to 57 weeks after injection did not show an elevation in serum pNF-H levels for the duration of the study as expected in SOD1-G93A mice with a life-time serum pNF-H average of 1,871.47 pg/mL and 1,600.99 pg/mL, respectively, highlighting the durability of this one-time treatment in preventing progression of phenotypes associated with neurodegeneration (Figure 5A).

Denervation of the neuromuscular junction in the hindlimbs is one of the first signs of disease pathophysiology observed in SOD1-G93A mice and can be measured as an electrophysiological decline in compound muscle action potential (CMAP).[26,27] Consistent with the pNF-H data, there was dose-dependent prevention of CMAP decreases in SOD1-G93A mice treated with AAV9-miR30a-SOD1 compared with mice treated with the non-targeting control, in which no CMAP decline was observed out to 57 weeks in the two highest dosed groups (8E+11GC and 16E+11GC) (Figure 5B), similar to what has been previously published for wild-type mice.[27] Moreover, mice treated with the non-targeting control showed a median life

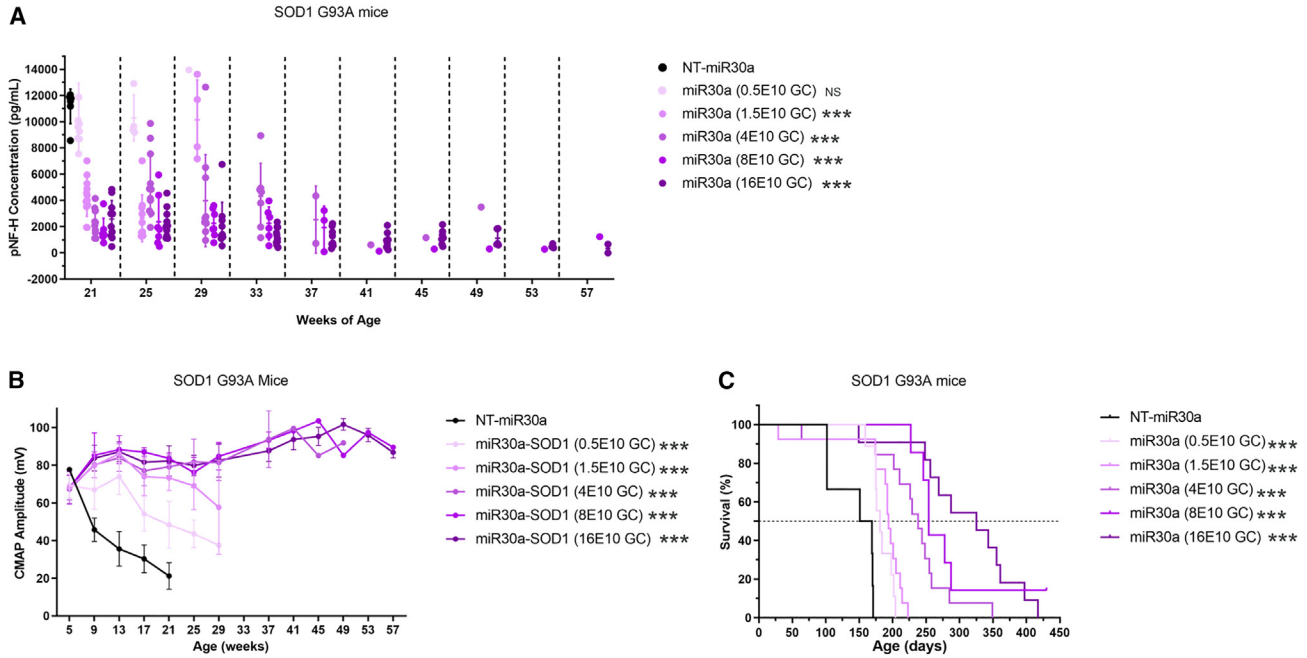

Figure 5. AAV9-miR30a-SOD1 can increase survival and reverse ALS-like phenotypes in SOD1-G93A mice

(A–C) P0 SOD1-G93A mice were given a one-time ICV injection of AAV9-miR30a-SOD1 at one of five dose levels (0.5E+10GC, 1.5E+10GC, 4.0E+10GC, 8.0E+10GC, or 16.0E+10GC), or an NT-miR30a control. A longitudinal measure of (A) serum pNF-H and (B) CMAP signaling. Data expressed as mean ± SD (n = 6–13). Generalized estimating equation was used to determine significance as compared with the NT-control ($^{NS}p > 0.05$, $^{***}p < 0.001$). (C) Survival of SOD1-G93A mice after amiR treatment (n = 6–13). Log rank test was used to determine significance as compared with the NT-control ($^{***}p < 0.001$).

span of 160 days, whereas mice treated with AAV9-miR30a-SOD1 had a significant increase in survival at a dose of either 0.5E+10GC, 1.5E+10GC, 4E+10GC, 8E+10GC, or 16E+10GC showing a median life span of 181, 194, 238, 254, or 325 days, respectively (Figure 5C). Overall, these data indicate that AAV9-miR30a-SOD1 can successfully reduce neurodegenerative events, maintain muscle strength and improve median life span of SOD1-G93A mice in a dose-dependent manner, suggesting it could be a viable treatment for SOD1-ALS based on our preclinical data.

DISCUSSION

In this study, we evaluated two pri-miRNA scaffolds (miR155 and miR30a) for their potential impact on the production and potency of a SOD1-targeting amiR when viral delivered by AAV9 in both *in vitro* and *in vivo* models. Compared with the miR155-based vector, an miR30a-based vector resulted in lower levels of guide strand production, in turn, seemed to be less potent at mediating SOD1 suppression *in vitro* and *in vivo*. However, the miR30a-based vector was well tolerated in mice and displayed only minimal to mild axonopathies in the dorsal funiculus of the spinal cord and sciatic nerve. In contrast, the miR155-based vector was less tolerated in mice, as evidenced by mild to moderate axonopathies, Purkinje cell loss in the cerebellum, and reduced life span observed after AAV9-miR155-SOD1 treatment. Finally, while AAV9-miR30a-SOD1 had lower guide strand production, it successfully prevented ALS-like phenotypes in SOD1-G93A mice and provided a robust survival benefit. This observation indicates that using the miR30a scaffold can minimize the risk of CNS-related toxicities compared with the miR155 scaffold while maintaining the desired efficacy in a preclinical model.

It has been recognized that using shRNAs and amiRs driven by Pol III promoters can result in various CNS-related toxicities, notably cerebellar Purkinje cell degeneration, and striatum abnormalities, after intraparenchymal injection of the AAV vectors.[16–18] These toxicities are thought to be caused by saturation of the miRNA machinery because of the high production of shRNAs or amiRs expressed from Pol III promoters.[15,17,18] Neither vector showed evidence of saturating the miRNA machinery in our study, as there was no detectable change in endogenous miRNA expression and no significant off-target transcriptional changes in the iPSC-derived NGN2 neurons upon transduction of AAV9-miR30a-SOD1 or AAV9-miR155-SOD1.[14] Cross-packaging of an AAV vector has also been reported as a source of toxicity in non-human primates.[28] However, we did not observe cross-packaging events with either of the vectors examined in this study (Figure S9).

One hypothesis is that the higher production of the amiR from the miR155 scaffold may induce strong immune-based responses due to the greater presence of foreign products. For example, the double-stranded RNA-sensing innate immune response can be triggered by the high amounts of a transgene from an AAV vector.[29] IsomiRs have also been shown to induce differentiating effects on the immune

response and gene silencing[30,31]; therefore, differences in isomiR formation observed between the miR155 and miR30a scaffolds could explain the contrasts in SOD1 silencing and tolerability. Furthermore, strong immune responses caused by unexpected expression from stuffer DNA sequences in an AAV vector in the cerebellum can elicit neurotoxic events in non-human primates, including Purkinje cell degeneration.[28] Similar Purkinje cell degeneration has been observed in mice treated with a shRNA-based AAV vector by Boudreau et al., and the authors speculated that this phenomenon might be caused by miRNA biogenesis pathway disruptions by highly expressed shRNAs whose unprocessed precursors thereby posed a burden to the cells.[17,32] Regardless of the underlying mechanism, Purkinje cells seem particularly susceptible to the unwanted by-products of RNAi therapies and could explain the observation of Purkinje cell loss in this study when mice were treated with the miR155-based vector that yielded approximately 10-fold more abundant amiR expression than the miR30a-based vector.

In addition, AAV9-miR155-SOD1 resulted in increased severity of axonal degeneration in the dorsal funiculus of the spinal cord and the sciatic nerve compared with mice treated with AAV9-miR30a-SOD1. Interestingly, this axonal degeneration is comparable with the pathology reported in non-human primates experiencing dorsal root ganglion toxicity after treatment with an AAV vector.[33–36] Therefore, we speculate these mice are experiencing similar AAV-induced toxicity, as this phenomenon has been recently described in rodents,[21] and we further hypothesize that the miR155 scaffold intensifies this pathology, relative to miR30a, because of its higher production. However, further analysis is required to confirm this hypothesis.

Finally, we showed that, while the miR30a-based vector led to lower amiR expression, it could still robustly increase survival, improve CMAP output, and lower pNF-H serum levels in SOD1-G93A mice in a dose-dependent manner. Considering the observed lower amiR expression with the miR30a scaffold, near 90% or greater suppression of SOD1 is achieved in mouse motor neurons. Therefore, the approximately 10-fold increase in amiR production by the miR155 scaffold would have a minimal impact on the target as the upper limit of suppression is nearly reached with the miR30a scaffold. In general, SOD1-targeting amiRs inserted into either a miR30a or miR155 scaffold have previously been described to reverse ALS-like phenotypes in SOD1-G93A mice.[8–10] Our data reaffirm previous findings regarding the benefits of using amiRs to potentially treat SOD1-ALS and further implies that miR30a may be a more optimal scaffold as it decreases the risk of adverse events compared with the miR155 scaffold while maintaining high therapeutic benefit in ALS mouse models.

This study examined only two amiR scaffolds as a proof of principle to show the impact scaffold selection can have on the efficacy and safety of an AAV-based RNAi therapeutic. As these therapies go into the clinic, it will be important to continually examine and optimize guide strand and amiR scaffold design to improve these therapeutics. For example, the miR33 scaffold has been recently shown to improve AAV genomic integrity compared with other amiR scaffolds.[15] Pri-miR scaffolds can impact guide strand selectivity and isomiR formation, which can all be influenced by stem length, loop size, and the presence of basal (CNNC and UG) and apical (UGU) sequences motifs.[37–39] In addition, the difference in sequence lengths of miR155 and miR30a scaffolds (132 and 319 bases, respectively) may influence amiR production and isomiR formation, which will need further investigation. Last, we reported higher guide/passenger ratios *in vivo* than *in vitro*, which could be related to the contrast in miRNA processing across species (i.e., mouse vs. human) and environments (i.e., whole tissue vs. cell culture), which has been previously reported.[40,41] Apart from optimizing scaffolds, it has been demonstrated that weaker promoters can reduce AAV-amiR-related toxicities and that AAV genotoxicity is influenced by age of injection, with older mice being less susceptible.[18,42] Overall, further optimization of pri-miRNA scaffolds, among other factors, is necessary for the development of ideal AAV-amiR-SOD1 gene therapy in the clinic.

This study highlights the significant impact of pri-miRNA scaffolds can have on amiR production and drug toxicity, even when the guide strands are the same and exhibit high specificity with no off-target effects. In particular, the higher production of the amiR embedded in the miR155 scaffold, compared with the miR30a scaffold, likely increased the risks for CNS-related toxicities (i.e., Purkinje cell loss). In conclusion, this work evaluated one aspect of RNAi gene therapy constructs and emphasized the importance of continuous assessment of different AAV construct components to optimize the potency, efficacy, and safety of these therapies as we attempt to translate them to the clinic for human use.

MATERIALS AND METHODS

AAV vector design, construction, and production

The designed single-stranded AAV9 vector contains a CAGG promoter that drives the expression of a mCherry protein, followed by an amiR targeting SOD1 in exon 5, the woodchuck hepatitis virus post-transcriptional regulatory element (WPRE), and a bovine hormone growth poly-A (bGH polyA) signal. The amiR coding sequence targeting both mouse and human SOD1 is based on the Invitrogen BLOCK-iT algorithm for the murine miR155 scaffold, while the human miR30a scaffold is based on Transomic shERWOOD algorithm.[43] The oligonucleotide sequence of both artificial miRNAs is listed as follows with the guide sequence underlined.miR155 construct: 5′-CTGGAGGCTTGCTGAAGGCTGTATGCTGTACTTTCTTCATTTCCACCTTGTTTTGGCCACTGACTGACAAGGTGGATGAAGAAAGTACAGGACACAAGGCCTGTTACTAGCACTCACATGGAACAAATGGCC-3′ miR30a construct: 5′-TGTTTGAATGAGGCTTCAGTACTTTACAGAATCGTTGCCTGCACATCTTGGAAACACTTGCTGGGATTACTTCTTCAGGTTAACCCAACAGAAGGCTAAAGAAGGTATATTGCTGTTGACAGTGAGCGTACTTTCTTCATTTCCACCTTTTAGTGAAGCCACAGATGTAAAGGTGGATGAAGAAAGTATGCCTACTGCCTCGGACTTCAAGGGGCTACTTTAGGAGCAATTATCTTGTTTACTAAAACTGAATACCTTGCTATCTCTTTGATACATTTTTACAAAGCTGAATTAAAATGGTATAAATTAAATCACTTTA-3′ PackGene Biotech produced AAV9-amiR vectors using

triple plasmid transfection protocol, as described previously.[44] Transmission electron microscopy and image analysis were conducted by Packgene to confirm minimal number of empty AAV capsids for each vector produced (Figure S10). AAV titers were quantified by ddPCR using a custom mCherry primer/probe (forward: 5′-TTGGACATCACCTCCCACAAC-3′; reverse: 5′-CCTCGGCGCGTTCGTA-3′; probe: 5′- 6FAM-ACTACACCATCGT GGAAC-MGB/NFQ-3′).

Intact genome analysis by 2D-ddPCR

AAV samples were treated with DNase I enzyme at 37°C for 30 min to remove non-encapsidated DNA. After DNase treatment, a propriety capsid lysis buffer was added to the samples, and they were treated at 60°C for 10 min to release the encapsidated genomes. Extracted genomes were combined with a duplex ddPCR master mix using ddPCR Supermix for Probes (no dUTP). Reactions were prepared with custom primer/probe sets targeting the CMV enhancer of the CAGG promoter and the bGH polyA. Percentages of intact genomes were determined by calculating the percentage of PCR-positive droplets that were positive for both the CMV enhancer and bGH polyA (Figure S11).

Animals

C57BL/6J (stock # 000664) mice and transgenic SOD1-G93A mice [B6.Cg-Tg(SOD1*G93A)/1Gur/J] (stock # 004435) were obtained from the Jackson Laboratories. Animals were randomized into treatment groups in all studies without considering any other variable. Experimenters were blind to treatment. Mice were housed in a 12/12 h light/dark cycle in a temperature-controlled room at 22°C–24°C, with access to food pellets and water provided *ad libitum*. All animal procedures were performed following the Biogen Institution Animal Care and Use Committee guidelines and the National Institute of Health *Guide for the Care and Use of Laboratory Animals*.

Neonatal intra-cerebroventricular injection

The intra-cerebroventricular (ICV) procedure was adapted from Torregrosa et al.[44] On P0, neonatal mice were anesthetized via hypothermia and injected with 4 μL AAV-RNAi vectors diluted in PBS with 0.25% Fast Green by a 33G needle, 10 μL, 45 beveled syringes (Hamilton). The injection site targets the lateral ventricle located laterally from the sagittal suture, midway between lambda and bregma, to a depth of 2 mm. Pups were recovered on a warm pad post-injection and returned to home cage until weaning at 4 weeks of age. P0 ICV injections were randomized and staggered for all treatment groups to minimize variation because of the timing of injection. Mice were only injected if they were within 24 h of age. Mice spinal cord and cortex were collected at ten weeks of age for bioanalytical and histological analysis.

iPSC-NGN2 cell culture

iPSC-NGN2 is a CRISPR-engineered wild-type iPSC line (ND07189) carrying a homozygous tet-inducible NGN2 expression cassette at the AAVS1 locus.[45] This stable iPSC line expressing NGN2 was induced by doxycycline for three days and frozen down on day 3 (D3) for future use. When D3 NGN2 neurons are plated, the day of seeding is called DIV 0 (days *in vitro*). The iPSC-NGN2 cells were plated on PDL-coated tissue culture plates (Corning 354470) and maintained in N2/B27 differentiation media (Life Technologies) with 200 μM ascorbic acid (Sigma), 1 μM dbcAMP (Sigma), 1 μg/mL doxycycline (Sigma), 10 μM CultureOne (Thermo Fisher), 10 ng/mL brain-derived neurotrophic factor (BDNF) (Tocris), and 10 ng/mL glial cell line-derived neurotrophic factor (GDNF) (R&D Systems) from DIV 0 to DIV 7. Cells were transduced with AAV-amiR vectors at 100,000 multiplicity of infection (MOI) on DIV 7 and were maintained in N2/B27 growth media with 200 μM ascorbic acid, 1 μM dbcAMP, 20 ng/mL BDNF, and 20 ng/mL GDNF from DIV 8 to DIV 21 in 37°C 5% CO_2 cell culture incubator. The growth medium was changed with one-half volume exchange on DIV 14. Cells were harvested on DIV 21 in QIAzol (Qiagen #79306) for RNA extraction using miRNeasy mini kit (Qiagen #217004).

Transduction efficiency *in vitro*

Immunofluorescence analysis of AAV-infected cells was performed on DIV 19, 16 days after infection. The number of mCherry positive cells were counted over the total number of Hoechst 33342-positive cells. Cells were fixed with 10% neutral buffer formalin (NBF) in PBS for 30 min at room temperature (RT), washed two times with DPBS, and incubated with 1% Triton X-100 (Invitrogen, catalog HFH10) in DPBS for 15 min at RT for permeabilization. Cells were blocked using Superblock T20 (Thermo Scientific, catalog 37536) for 1 h at RT. Plates were then stained with Hoechst 33342 (Invitrogen, catalog H3570) and incubated for 1 h at RT in the dark. After washing two times with PBS, confocal images were taken using an Opera Phenix High-Content Screening system (PerkinElmer) equipped with Harmony software (version 4.9) at 40× objective and analyzed by Columbus software (version 2.9.1).

Mouse cortical neuron culture transduction and immunoblotting

Primary cortical neurons were isolated from embryonic day 16 Cas9−/+; SOD1-G93A−/+ mouse embryos. Cells were dissociated by using 20 U/mL papain (Worthington) and seeded at a density of 9 E4 cells per well in 24-well plate coated with 0.5 mg/mL poly-D-lysine (P7886, Sigma) and 2.5 g/mL laminin (Invitrogen). Dissociated cells were cultured overnight in DMEM with 10% FBS, 1% penicillin-streptomycin (pen-strep) for recovery, and subsequently maintained in neurobasal medium (Invitrogen) supplemented with 2% B27 (Invitrogen), 1% pen-strep, and 1% GlutaMAX (Invitrogen). On DIV 5, dissociated cortical neuron cultures were transduced with AAV-miR155 and AAV-miR30a at 1E5GC MOI and harvested on DIV 15 for SDS-PAGE and Western blot analysis. Cells were lyzed in Novex Tris-Glycine SDS sample buffer with NuPAGE sample reducing agent (Invitrogen). Cell lysates were separated on Novex Tris-Glycine gels, transferred to nitrocellulose membrane, and probed with primary antibodies, against β-actin (926-42210, LI-COR Biosciences) and SOD1 (ADI-SOD1-100, Enzo) at 4°C overnight. The IRDye 800CW-conjugated and IRDye 680-conjugated secondary antibodies (LI-COR Biosciences) were used and detected by the Odyssey CLx infrared imaging system. Immunoblot band intensities were analyzed by ODYSSEY application software (LI-COR Biosciences).

RNA-seq and next-generation sequencing analysis

Small RNA-seq libraries were prepared from 100ng of total RNA using the forward strand-specific QIAseq miRNA Library Kit (#331505) with QIAseq miRNA 96 Index IL kit (#331565) according to the manufacturer's protocol. Libraries were pooled and sequenced on a HiSeq 2500 (Illumina) SR flowcell to generate 75-bp single-end reads. A total of 6–13 million reads were generated per sample. The miRNA-seq data were analyzed with the QuickMIRSeq pipeline.[46] Briefly, the reads from multiple lanes were merged, then trimmed on both ends using cutadapt version 1.11.[47] A reference database was created by merging the miRBase Sequence Database Release 22.1 with manually created entries for the artificial miRNAs.[48] Reference sequences of different RNA species were used to quantify the relative amounts of miRNA versus other types of transcripts in the samples. References for spliced mRNA and non-coding RNA types were downloaded from ENSEMBL, while transfer RNA (tRNA) reference sequences were obtained from the tRNAscan-SE Genomic tRNA Database.[49,50] The alignment against these references was done with bowtie version 0.12.7.[51] Custom shell, R, and Perl scripts were used to compute metrics for artificial miRNAs: guide-to-passenger ratio, percentages relative to total endogenous miRNA amounts, fraction of accurately expressed sequences, and the number of unprocessed hairpin loops. Total guide and passenger strands were calculated to include the total pool of isomiRs. Differential expression analysis performed with DESeq2 version 1.30.0.[52]

RNA-seq libraries were generated from 500 ng total RNA using the KAPA mRNA HyperPrep Kit (Roche) according to manufacturer's instructions. NGN2 libraries were sequenced on a NextSeq 550 1 × 50 bp to an average depth of 16m fragments per sample. Mouse tissue libraries were sequenced on a HiSeq 2500 1 × 50 bp, with an average depth of 25m fragments per sample. DESeq2 pipeline was used to find differentially expressed transcripts for samples with sequencing depth from 20 to 30 million reads were generated per sample. The fastq files were generated from the bcl files using bcl2fastq v2.20 (Illumina). The RNA-seq analysis pipeline consisted of alignment with STAR version 2.5.2a against human genome version GRCh38 and Gencode gene model release 27 for NGN2 dataset, and the mouse genome version GRCm38, Genecode model release M25, for mouse dataset.[53,54] After alignment, quantification of gene expression was carried out with RSEM v1.2.26.[55] Differential expression analysis was performed with DESeq2 version 1.30.0.[52]

RNA isolation and two-step RT-qPCR

Mouse spinal cord and cortex were pulverized using one 6 mm steel bead in a cryogenic Genogrinder (Spex Sample Prep) at a speed of 1,000–1,200 strokes/min for 30–40 s and subsequently homogenized in QIAzol (Qiagen #79306) using Bead Ruptor (Omni #19-050A) for two cycles at a speed of 5.62 m/s, 30 s per cycle. The cultured iPSC-NGN2 cells were pipetted up and down and fully lysed in QIAzol. RNA was isolated using miRNeasy mini kit (Qiagen #217004) following the manufacturer's protocol, including on-column DNase digestion.

Total RNA concentration was fluorescently measured using the Quant-IT RNA assay kit (Thermo Fisher Scientific #Q33140). The integrity of RNA was assessed by measuring the RNA integrity number using the HT RNA Reagent kit, HT Lab Chip kit, and GXII Touch Instrument (PerkinElmer #CLS153530 and #760435, respectively). The cDNA was synthesized using a High-Capacity cDNA reverse transcription kit (Applied Biosystems #4368814). qPCR was performed on Quantstudio 12K Flex PCR system using 20 ng cDNA per reaction well combined with TaqMan Fast Advanced Master Mix (Thermo Fisher Scientific #4444556) and the Taqman probes (Applied Biosystems) for housekeeping genes (VIC/MGB) and target genes (FAM/MGB) listed below. For iPSC-NGN2 cells, human GAPDH (Hs99999905_m1) and custom probes targeting human SOD1 exon 4 (forward 5′-TGGTGTGGCCGATGTGTCTA-3′, reverse 5′-ATGATGCAATGGTCTCCTGAGA-3′, probe 5′-6FAM-TGAAGATTCTGTGATCTCA-MGB/NFQ-3′) were used in Figure 1C. For wild-type spinal cord and cortex, mouse GAPDH (Mm99999915_g1) and mouse SOD1 (Mm01344233_g1) probes were used in Figure 2B. Expression of SOD1 was normalized to vehicle-treated control (for mouse tissue) or non-targeting control (for iPSC-NGN2) and analyzed relative to mouse or human GAPDH using the comparative $2^{-\Delta\Delta CT}$ method, as described previously.[56]

DNA isolation and biodistribution by ddPCR for iPSC-NGN2

DIV19 iPSC-NGN2 7189 L cells were rinsed with 1× PBS before DNA extraction. MagMax Multi-sample DNA extraction kit (Thermo Fisher Scientific) was adapted to KingFisher Flex System for DNA extraction following the manufacturer's instructions. Cells were lyzed by DNA lysis buffer and proteinase K mixture and incubated at 60°C overnight with shaking at 300 RPM. Cell homogenate was transferred to a 96-well deep-well plate. We added 300 µL of 100% isopropanol and 40 µL of DNA Binding Bead Mix to the homogenate sequentially. DNA was eluted in Elution Buffer after subsequent wash and RNase mixture incubation steps. Total DNA concentration was determined with NanoDrop 8000 (Thermo Fisher Scientific).

We analyzed 5 µL of the eluted DNA or 1:5 dilution of the eluted DNA for viral DNA and gDNA quantifications by ddPCR as duplex. Custom primers and probes targeting human RPP30 were from Integrated DNA Technology (Coralville, Iowa). Primers and probe for analyzing human RPP30 (ribonuclease P protein subunit p30) are as follows: forward 5′-CTGAGAAGGGACTACCCTAGAA-3′, reverse 5′-CTGCTTGACCACACAGGTAT-3′, and probe 5′-/5HEX/ACCCTGCTG/ZEN/ACCTTTCATTCCTCC/3IABkFQ/-3′. Custom primers and probe targeting WPRE (Woodchuck Hepatitis Virus) were obtained from Thermo Fisher Scientific (forward 5′-TGTTGCTCCTTTTACGCTATGTG-3′, reverse 5′-CGGGAAGCAATAGCATGATACA-3', and probe 5′-6FAM-ATACGCTGCTTTAATGC-MGB/NFQ-3′) The 25 µL ddPCR reaction mixture was composed of 12.5 µL of 2× ddPCR Supermix for probes (No dUTP) (Bio-Rad), 0.75 µL WPRE-FAM, 0.75 µL hRPP30-HEX probes (900 nM primers and 250 nM probe at final concentration), 6 µL nuclease-free water, and 5 µL DNA sample. Droplets were generated with the automated droplet generator and temperature cycling with conditions of 10 min at 95°C and 40 cycles of 30 s at 94°C

and 1 min at 60°C and 1 final cycle of 10 min at 98°C. Droplets were read by the QX200 droplet reader (Bio-Rad). Data was analyzed using QX Manager software, version 1.2 standard edition (Bio-Rad). The copy numbers of the viral DNA were the absolute copy number derived from ddPCR. The unit reported from ddPCR assay for viral DNA quantification was viral genome (vg)/diploid genome of human RPP30 (dg), which is vg copy number/0.5 * haploid hRPP30 copy number. The reported vg/dg values are under the assumption that the DNA extraction efficiency between viral DNA and gDNA is similar, and between two scaffolds is similar as well.

DNA isolation and biodistribution by qPCR for mouse tissues

Pulverized mouse spinal cord and cortex samples were subjected to tissue lysis, digestion, and DNA extraction procedures using DNeasy 96 Blood & Tissue Kit from Qiagen. ATL and proteinase K buffer were added to the wells and homogenates were incubated at 56°C with shaking at 225 RPM with ThermoMixer C overnight. We added 4 μL 100 mg/mL RNAse A (Qiagen) to each well before proceeding to subsequent DNA extraction procedures following manufacturer's instruction. All the centrifugation steps were performed with Sigma 4-16KS centrifuge at 6,000×*g* (Qiagen). DNA was eluted in AE buffer and total DNA concentration was determined with NanoDrop 8000 (Thermo Fisher Scientific). Each eluted DNA sample was normalized to 20 ng/μL with nuclease-free water for qPCR analysis. Sample DNA (20 ng/reaction) and pre-validated linearized plasmid standards containing WPRE and mouse RPP30 sequence (0, 1, 5, 10, 50, 100, 1E3, 1E4, 1E5, 1E6, 1E7, or 1E8 copies/reaction) was analyzed by qPCR (10 μL/reaction) in a 384-well optical plate using custom TaqMan primer/probe sets specific for both vector DNA and mouse genomic DNA at final concentration of 890 nM for primers and 247.5 nM for probes in triplicates with TaqMan Universal PCR Master Mix, no AmpErase UNG (Applied Biosystems, NJ) on CFX384 system (Bio-Rad). Viral vector DNA detection was obtained via detecting WPRE-FAM and mouse gDNA quantification was obtained by detecting RPP30-HEX. Measurements of viral vector DNA and gDNA were performed as a duplex assay. PRC cycling conditions were 10 min at 95°C, 40 cycles of 15 s at 95°C, and 1 min at 60°C. The quantity of the viral DNA and the genomic DNA were interpolated from the standard curve prepared. Amplification efficiency (E) was calculated with the following equation: $E = -1 + 10^{(-1/S)}$, in which S is the slope of the standard curve. The unit reported from this qPCR assay for viral DNA quantification was vg/diploid genome of RPP30 (dg), which is vg copy number/0.5 * haploid RPP30 copy number.

RNAscope *in situ* hybridization

The lumbar spinal cord was fixed in 10% neutral buffered formalin (NBF) for 72 h, processed and embedded in paraffin. Two 5-μm-thick sections were collected from three different levels of lumbar spinal cord, separated by more than 75 μm apart. Chromogenic dual RNAScope (Advanced Cell Diagnostics [ACD]) *in situ* hybridization was performed according to manufacturer's instruction using Leica BondRX automated staining platform. Probes against target MmSOD1 (Cat. #812968-C1) and a motor neuron marker MmChAT (Cat. #408738-C2) were obtained from ACD. RNAscope 2.5 LS Duplex Red/Brown Reagent Kit was used (ACD, Cat. No. 322440). Slides were scanned on a Panoramic P250 scanner using a 40× objective. The ventral horn area was hand annotated on each spinal cord section and validated by comparison with an anatomical atlas. Motor neurons were segmented with an AI-based algorithm using Visiopharm software. Quantification of SOD1 RNAscope signal was achieved by using color deconvolution filters to separate red and brown chromogens.

Hematoxylin and eosin staining and pathology scoring

Mouse brain, spinal cord, and sciatic nerve tissues were fixed in 10% NBF. Whole brain tissue was trimmed at four different levels ([1] cerebrum at the level of lateral ventricles, [2] cerebrum at the level of the hippocampus and thalamus, [3] brainstem, and [4] cerebellum). Once trimmed, trimmed sections were paraffin embedded together and sectioned on one slide in a coronal plane. One brain region (medulla) and three spinal cord regions ([1] cervical, [2] thoracic, and [3] lumbar) were trimmed. Trimmed sections of medulla and spinal cord were paraffin embedded together and sectioned onto one slide in a transverse plane. Sciatic nerve was paraffin embedded and sectioned on a single slide in a sagittal plane. We stained 5-μm-thick sections with H&E. Samples were stained in different batches which could cause batch-to-batch variability in stain intensity. H&E slides were evaluated visually and assessed for severity of histopathological changes on a scale of 0–5 (0 = no change, 1 = minimal change, 2 = mild change, 3 = moderate change, 4 = marked change, 5 = severe change). Severity scores were based on one slide containing either four different regions of the brain or spinal cord, or the length of the sciatic nerve. Description of histopathologic scoring criteria is provided in the Tables S1—S3. Samples were either imaged at Charter Preclinical Services or Biogen.

Survival study guideline

Daily body weight and paralysis were monitored for the SOD1-G93A mice after 130–140 days of age or as soon as onset of the disease phenotype was observed. Dietgel, Hydrogel, and dry food pellets were supplemented daily. Subcutaneous fluids (1 mL) were provided if dehydration was observed. The parameters measured for a humane endpoint for animal euthanization included a loss of more than 20% of peak body weight and the inability to return to a quadruple position within 15 s after being placed on the side.

CMAP

Experimenters were blind to genotype and treatment conditions. CMAP recordings were performed at the indicated time points (weeks 5–57 in Figure 5B) under isoflurane (1.5%–2.5%) anesthesia and with body temperature maintained at 37°C. Adequate anesthesia was confirmed in the absence of a pain withdrawal reflex upon mild pressure on the hindlimb. Disposable monopolar 28G needle electrodes (Teca 25 mm, 28G electrodes, Natus Medical Inc.) were used for stimulation and recording. The sciatic nerve was stimulated near the sciatic notch with constant-current monophasic square-wave pulses started at 1.0 mA and increased at 0.5 mA increment.

Each stimulation was 0.1 ms in duration and delivered every 2 s. For CMAP recordings, the recording electrode was placed intramuscularly 1 mm deep in the tibialis anterior. Stimulation current was increased until the amplitude of CMAP had reached a maximum, known as supramaximal stimulus (1.5–3.5 mA). Recordings were performed using a current level of 0.5 mA above this value. The amplitude of maximum peak to minimum peak of the biphasic CMAP waveform was recorded after 0.8 ms of stimulation to exclude the latency from the initiation of stimulus to the initiation of the response. For each animal, right and left leg amplitudes were averaged for the CMAP value.

Serum neurofilament assessment

Approximately 100 μL whole blood was sampled every 4 weeks at the indicated time point (weeks 5 and 9 in Figure 4A; weeks 21–57 in Figure 5A) by facial vein puncture and stored in BD Microtainer SST Clog Activator/Gel tubes (Becton Dickinson). The collected blood was centrifugated at 2000RCF (4,600 RPM) for 10 min to isolate serum for measurement of pNF-H. Levels of pNF-H in serum were quantified by pNF-H kit (Protein Simple, SPCKB-PS-000519) and the ELLA microfluidic ELISA platform following the manufacturer's protocol.

Statistical analysis

Welch's one-way ANOVA was performed to compare means between multiple groups, followed by post hoc pairwise t-tests using Holm's method for adjusting multiple comparisons. Longitudinal data were analyzed using generalized estimating equation to assess group differences while controlling for time. Log rank tests were used to determine statistical significance of mouse survival data. All analyses were run in R version 4.1.2 and GraphPad Prism version 9.2.0. Statistical significance was called at the 0.05 level.

DATA AND CODE AVAILABILITY

Data are available upon request.

ACKNOWLEDGMENTS

Funding supporting this research was provided by Biogen, Cambridge, MA, USA. The authors would like to acknowledge Kay-Ellen (Kate) Chicoine from Biogen, Cambridge, MA, USA for her support and collection of histopathological images related to this study. The authors would like to acknowledge Deborah Y. Kwon from Biogen, Cambridge, MA, USA for her assistance on the graphical abstract.

AUTHOR CONTRIBUTIONS

S.K.C. and Z.C.E.H. wrote the manuscript with input from co-authors; S.K.C., S.Hana, D.F., S.X., S.Hamann, G.M., P.C., R.C., T.C., K.K., W.L., A.P., P.C., C.W., and S.C.L. performed the research; M.Z., B.G., M.H., S.K.C., Z.C.E.H., H.Z., F.G., and S.C.L. performed data analysis; S.C.L .supervised the project and writing of this manuscript; S.K.C. and Z.C.E.H. contributed equally and can switch listed first author for CV purposes.

DECLARATION OF INTERESTS

M.H. is a paid advisor from Charter Preclinical Services. All other authors are paid employees at Biogen.

REFERENCES

1. Oskarsson, B., Gendron, T.F., and Staff, N.P. (2018). Amyotrophic Lateral Sclerosis: An Update for 2018. Mayo Clin. Proc. *93*, 1617–1628.
2. Rosen, D.R., Siddique, T., Patterson, D., Figlewicz, D.A., Sapp, P., Hentati, A., Donaldson, D., Goto, J., O'Regan, J.P., Deng, H.X., et al. (1993). Mutations in Cu/Zn superoxide dismutase gene are associated with familial amyotrophic lateral sclerosis. Nature *362*, 59–62.
3. Kim, G., Gautier, O., Tassoni-Tsuchida, E., Ma, X.R., and Gitler, A.D. (2020). ALS Genetics: Gains, Losses, and Implications for Future Therapies. Neuron *108*, 822–842.
4. Oeda, T., Shimohama, S., Kitagawa, N., Kohno, R., Imura, T., Shibasaki, H., and Ishii, N. (2001). Oxidative stress causes abnormal accumulation of familial amyotrophic lateral sclerosis-related mutant SOD1 in transgenic Caenorhabditis elegans. Hum. Mol. Genet. *10*, 2013–2023.
5. Siddique, T., Nijhawan, D., and Hentati, A. (1997). Familial amyotrophic lateral sclerosis. J. Neural. Transm. Suppl. *49*, 219–233.
6. Şahin, A., Held, A., Bredvik, K., Major, P., Achilli, T.M., Kerson, A.G., Wharton, K., Stilwell, G., and Reenan, R. (2017). Human SOD1 ALS Mutations in a Drosophila Knock-In Model Cause Severe Phenotypes and Reveal Dosage-Sensitive Gain- and Loss-of-Function Components. Genetics *205*, 707–723.
7. Kong, J., and Xu, Z. (1998). Massive mitochondrial degeneration in motor neurons triggers the onset of amyotrophic lateral sclerosis in mice expressing a mutant SOD1. J. Neurosci. *18*, 3241–3250.
8. Stoica, L., Todeasa, S.H., Cabrera, G.T., Salameh, J.S., ElMallah, M.K., Mueller, C., Brown, R.H., Jr., and Sena-Esteves, M. (2016). Adeno-associated virus-delivered artificial microRNA extends survival and delays paralysis in an amyotrophic lateral sclerosis mouse model. Ann. Neurol. *79*, 687–700.
9. Li, D., Liu, C., Yang, C., Wang, D., Wu, D., Qi, Y., Su, Q., Gao, G., Xu, Z., and Guo, Y. (2017). Slow Intrathecal Injection of rAAVrh10 Enhances its Transduction of Spinal Cord and Therapeutic Efficacy in a Mutant SOD1 Model of ALS. Neuroscience *365*, 192–205.
10. Wang, H., Yang, B., Qiu, L., Yang, C., Kramer, J., Su, Q., Guo, Y., Brown, R.H., Jr., Gao, G., and Xu, Z. (2014). Widespread spinal cord transduction by intrathecal injection of rAAV delivers efficacious RNAi therapy for amyotrophic lateral sclerosis. Hum. Mol. Genet. *23*, 668–681.
11. Miller, T., Cudkowicz, M., Shaw, P.J., Andersen, P.M., Atassi, N., Bucelli, R.C., Genge, A., Glass, J., Ladha, S., Ludolph, A.L., et al. (2020). Phase 1–2 Trial of Antisense Oligonucleotide Tofersen for SOD1 ALS. N. Engl. J. Med. *383*, 109–119.
12. Mueller, C., Berry, J.D., McKenna-Yasek, D.M., Gernoux, G., Owegi, M.A., Pothier, L.M., Douthwright, C.L., Gelevski, D., Luppino, S.D., Blackwood, M., et al. (2020). SOD1 Suppression with Adeno-Associated Virus and MicroRNA in Familial ALS. N. Engl. J. Med. *383*, 151–158.
13. Kotowska-Zimmer, A., Pewinska, M., and Olejniczak, M. (2021). Artificial miRNAs as Therapeutic Tools: Challenges and Opportunities, *12* (Wiley Interdiscip Rev RNA), p. e1640.
14. Borel, F., Kay, M.A., and Mueller, C. (2014). Recombinant AAV as a Platform for Translating the Therapeutic Potential of RNA Interference. Mol. Ther. *22*, 692–701.
15. Grimm, D., Streetz, K.L., Jopling, C.L., Storm, T.A., Pandey, K., Davis, C.R., Marion, P., Salazar, F., and Kay, M.A. (2006). Fatality in mice due to oversaturation of cellular microRNA/short hairpin RNA pathways. Nature *441*, 537–541.
16. Xie, J., Tai, P.W.L., Brown, A., Gong, S., Zhu, S., Wang, Y., Li, C., Colpan, C., Su, Q., He, R., et al. (2020). Effective and Accurate Gene Silencing by a Recombinant AAV-Compatible MicroRNA Scaffold. Mol. Ther. *28*, 422–430.
17. Boudreau, R.L., Martins, I., and Davidson, B.L. (2009). Artificial microRNAs as siRNA shuttles: improved safety as compared to shRNAs in vitro and in vivo. Mol. Ther. *17*, 169–175.
18. Pfister, E.L., Chase, K.O., Sun, H., Kennington, L.A., Conroy, F., Johnson, E., Miller, R., Borel, F., Aronin, N., and Mueller, C. (2017). Safe and Efficient Silencing with a Pol

II, but Not a Pol lII, Promoter Expressing an Artificial miRNA Targeting Human Huntingtin. Mol. Ther. Nucleic Acids *7*, 324–334.

19. Zhou, H., Arcila, M.L., Li, Z., Lee, E.J., Henzler, C., Liu, J., Rana, T.M., and Kosik, K.S. (2012). Deep annotation of mouse iso-miR and iso-moR variation. Nucleic Acids Res. *40*, 5864–5875.
20. Foust, K.D., Nurre, E., Montgomery, C.L., Hernandez, A., Chan, C.M., and Kaspar, B.K. (2009). Intravascular AAV9 preferentially targets neonatal-neurons and adult-astrocytes in CNS. Nat. Biotechnol. *27*, 59–65.
21. Fader, K.A., Pardo, I.D., Kovi, R.C., Somps, C.J., Wang, H.H., Vaidya, V.S., Ramaiah, S.K., and Sirivelu, M.P. (2022). Circulating neurofilament light chain as a promising biomarker of AAV-induced dorsal root ganglia toxicity in nonclinical toxicology species. Mol. Ther. Methods Clin. Dev. *25*, 264–277.
22. Yuan, R., Tsaih, S.W., Petkova, S.B., Marin de Evsikova, C., Xing, S., Marion, M.A., Bogue, M.A., Mills, K.D., Peters, L.L., Bult, C.J., et al. (2009). Aging in inbred strains of mice: study design and interim report on median lifespans and circulating IGF1 levels. Aging Cell *8*, 277–287.
23. McCombe, P.A., Pfluger, C., Singh, P., Lim, C.Y.H., Airey, C., and Henderson, R.D. (2015). Serial measurements of phosphorylated neurofilament-heavy in the serum of subjects with amyotrophic lateral sclerosis. J. Neurol. Sci. *353*, 122–129.
24. Steinacker, P., Feneberg, E., Weishaupt, J., Brettschneider, J., Tumani, H., Andersen, P.M., von Arnim, C.A.F., Böhm, S., Kassubek, J., Kubisch, C., et al. (2016). Neurofilaments in the diagnosis of motoneuron diseases: a prospective study on 455 patients. J. Neurol. Neurosurg. Psychiatry *87*, 12–20.
25. Lu, C.H., Petzold, A., Kalmar, B., Dick, J., Malaspina, A., and Greensmith, L. (2012). Plasma neurofilament heavy chain levels correlate to markers of late stage disease progression and treatment response in SOD1(G93A) mice that model ALS. PLoS One *7*, e40998.
26. Mancuso, R., Osta, R., and Navarro, X. (2014). Presymptomatic electrophysiological tests predict clinical onset and survival in SOD1(G93A) ALS mice. Muscle Nerve *50*, 943–949.
27. McCampbell, A., Cole, T., Wegener, A.J., Tomassy, G.S., Setnicka, A., Farley, B.J., Schoch, K.M., Hoye, M.L., Shabsovich, M., Sun, L., et al. (2018). Antisense oligonucleotides extend survival and reverse decrement in muscle response in ALS models. J. Clin. Invest. *128*, 3558–3567.
28. Keiser, M.S., Ranum, P.T., Yrigollen, C.M., Carrell, E.M., Smith, G.R., Muehlmatt, A.L., Chen, Y.H., Stein, J.M., Wolf, R.L., Radaelli, E., et al. (2021). Toxicity after AAV delivery of RNAi expression constructs into nonhuman primate brain. Nat. Med. *27*, 1982–1989.
29. Shao, W., Earley, L.F., Chai, Z., Chen, X., Sun, J., He, T., Deng, M., Hirsch, M.L., Ting, J., Samulski, R.J., and Li, C. (2018). Double-stranded RNA innate immune response activation from long-term adeno-associated virus vector transduction. JCI Insight *3*, e120474.
30. Al-Modawi, R.N., Brinchmann, J.E., and Karlsen, T.A. (2021). Extensive downregulation of immune gene expression by microRNA-140-3p 5' isomiR in an in vitro model of osteoarthritis. Osteoarthr. Cartil. Open *3*, 100189.
31. Bofill-De Ros, X., Kasprzak, W.K., Bhandari, Y., Fan, L., Cavanaugh, Q., Jiang, M., Dai, L., Yang, A., Shao, T.J., Shapiro, B.A., et al. (2019). Structural differences between pri-miRNA paralogs promote alternative drosha cleavage and expand target repertoires. Cell Rep. *26*, 447–459.e4.
32. Mcbride, J.L., Boudreau, R.L., Harper, S.Q., Staber, P.D., Monteys, A.M., Martins, I., Gilmore, B.L., Burstein, H., Peluso, R.W., Polisky, B., et al. (2008). Artificial miRNAs mitigate shRNA-mediated toxicity in the brain: implications for the therapeutic development of RNAi. Proc. Natl. Acad. Sci. USA *105*, 5868–5873.
33. Hinderer, C., Katz, N., Buza, E.L., Dyer, C., Goode, T., Bell, P., Richman, L.K., and Wilson, J.M. (2018). Severe Toxicity in Nonhuman Primates and Piglets Following High-Dose Intravenous Administration of an Adeno-Associated Virus Vector Expressing Human SMN. Hum. Gene Ther. *29*, 285–298.
34. Hordeaux, J., Buza, E.L., Dyer, C., Goode, T., Mitchell, T.W., Richman, L., Denton, N., Hinderer, C., Katz, N., Schmid, R., et al. (2020). Adeno-Associated Virus-Induced Dorsal Root Ganglion Pathology. Hum. Gene Ther. *31*, 808–818.
35. Hordeaux, J., Buza, E.L., Jeffrey, B., Song, C., Jahan, T., Yuan, Y., Zhu, Y., Bell, P., Li, M., Chichester, J.A., et al. (2020). MicroRNA-mediated inhibition of transgene expression reduces dorsal root ganglion toxicity by AAV vectors in primates. Sci. Transl. Med. *12*, eaba9188.
36. Tukov, F.F., Mansfield, K., Milton, M., Meseck, E., Penraat, Chand, D., and Hartmann, A. (2022). Single-dose intrathecal dorsal root ganglia toxicity of onasemnogene abeparvovec in cynomolgus monkeys. Hum. Gene Ther. *33*, 740–756.
37. Miniarikova, J., Zanella, I., Huseinovic, A., Van der Zon, T., Hanemaaijer, E., Martier, R., Koornneef, A., Southwell, A.L., Hayden, M.R., Van Deventer, S.J., et al. (2016). Design, Characterization, and Lead Selection of Therapeutic miRNAs Targeting Huntingtin for Development of Gene Therapy for Huntington's Disease. Mol. Ther. Nucleic Acids *5*, e297.
38. Fang, W., and Bartel, D.P. (2015). The menu of features that define primary microRNAs and enable de novo design of microRNA genes. Mol. Cell *60*, 131–145.
39. Galka-Marciniak, P., Olejniczak, M., Starega-Roslan, J., Szczesniak, M.W., Makalowska, I., and Krzyzosiak, W.J. (2016). siRNA release from pri-miRNA scaffolds is controlled by the sequence and structure of RNA. Biochim. Biophys. Acta *1859*, 639–649.
40. Guo, L., Zhao, Y., Zhang, H., Yang, S., and Chen, F. (2013). Close association between paralogous multiple isomiRs and paralogous/orthologues miRNA sequences implicates dominant sequence selection across various animal species. Gene *527*, 624–629.
41. Kuosmanen, S.M., Kansanen, E., Sihvola, V., and Levonen, A.L. (2017). MicroRNA Profiling Reveals Distinct Profiles for Tissue-Derived and Cultured Endothelial Cells. Sci. Rep. *7*, 10943.
42. Chandler, R.J., LaFave, M.C., Varshney, G.K., Trivedi, N.S., Carrillo-Carrasco, N., Senac, J.S., Wu, W., Hoffmann, V., Elkahloun, A.G., Burgess, S.M., and Venditti, C.P. (2015). Vector design influences hepatic genotoxicity after adeno-associated virus gene therapy. J. Clin. Invest. *125*, 870–880.
43. Knott, S.R.V., Maceli, A., Erard, N., Chang, K., Marran, K., Zhou, X., Gordon, A., Demerdash, O.E., Wagenblast, E., Kim, S., et al. (2014). A computational algorithm to predict shRNA potency. Mol. Cell *56*, 796–807.
44. Torregrosa, T., Lehman, S., Hana, S., Marsh, G., Xu, S., Koszka, K., Mastrangelo, N., McCampbell, A., Henderson, C.E., and Lo, S.C. (2021). Use of CRISPR/Cas9-mediated disruption of CNS cell type genes to profile transduction of AAV by neonatal intracerebroventricular delivery in mice. Gene Ther. *28*, 456–468.
45. Wang, C., Ward, M.E., Chen, R., Liu, K., Tracy, T.E., Chen, X., Xie, M., Sohn, P.D., Ludwig, C., Meyer-Franke, A., et al. (2017). Scalable Production of iPSC-Derived Human Neurons to Identify Tau-Lowering Compounds by High-Content Screening. Stem Cell Rep. *9*, 1221–1233.
46. Zhao, S., Gordon, W., Du, S., Zhang, C., He, W., Xi, L., Mathur, S., Agostino, M., Paradis, T., von Schack, D., et al. (2017). QuickMIRSeq: a pipeline for quick and accurate quantification of both known miRNAs and isomiRs by jointly processing multiple samples from microRNA sequencing. BMC Bioinf. *18*, 180.
47. Martin, M. (2011). Cutadapt removes adapter sequences from high-throughput sequencing reads. EMBnet. j. *17*, 10.
48. Kozomara, A., Birgaoanu, M., and Griffiths-Jones, S. (2019). miRBase: from microRNA sequences to function. Nucleic Acids Res. *47*, D155–D162.
49. Yates, A.D., Achuthan, P., Akanni, W., Allen, J., Allen, J., Alvarez-Jarreta, J., Amode, M.R., Armean, I.M., Azov, A.G., Bennett, R., et al. (2020). Ensembl 2020. Nucleic Acids Res. *48*, D682–D688.
50. Chan, P.P., and Lowe, T.M. (2016). GtRNAdb 2.0: an expanded database of transfer RNA genes identified in complete and draft genomes. Nucleic Acids Res. *44*, D184–D189.
51. Langmead, B., Trapnell, C., Pop, M., and Salzberg, S.L. (2009). Ultrafast and memory-efficient alignment of short DNA sequences to the human genome. Genome Biol. *10*, R25.
52. Love, M.I., Huber, W., and Anders, S. (2014). Moderated estimation of fold change and dispersion for RNA-seq data with DESeq2. Genome Biol. *15*, 550.
53. Frankish, A., Diekhans, M., Ferreira, A.M., Johnson, R., Jungreis, I., Loveland, J., Mudge, J.M., Sisu, C., Wright, J., Armstrong, J., et al. (2019). GENCODE reference annotation for the human and mouse genomes. Nucleic Acids Res. *47*, D766–D773.
54. Dobin, A., and Gingeras, T.R. (2016). Optimizing RNA-Seq Mapping with STAR. Methods Mol. Biol. *1415*, 245–262.
55. Li, B., and Dewey, C.N. (2011). RSEM: accurate transcript quantification from RNA-Seq data with or without a reference genome. BMC Bioinf. *12*, 323.
56. Livak, K.J., and Schmittgen, T.D. (2001). Analysis of relative gene expression data using real-time quantitative PCR and the 2(-Delta Delta C(T)) Method. Methods *25*, 402–408.